

# Geochemistry, Geophysics, Geosystems®



## RESEARCH ARTICLE

10.1029/2022GC010544

### Key Points:

- Strong lattice-preferred orientation develops across the coesite-stishovite transition at mantle conditions
- 10–50 vol.% mid-ocean ridge basalt mixed with pyrolyte explains the impedance contrast of the X-discontinuity
- Intermittent visibility of the X-discontinuity can be explained by probing geometry

### Supporting Information:

Supporting Information may be found in the online version of this article.

### Correspondence to:

M. Krug,  
[krugma@uni-muenster.de](mailto:krugma@uni-muenster.de)












### Citation:

Krug, M., Saki, M., Ledoux, E., Gay, J. P., Chantel, J., Pakhomova, A., et al. (2022). Textures induced by the coesite-stishovite transition and implications for the visibility of the X-discontinuity. *Geochemistry, Geophysics, Geosystems*, 23, e2022GC010544. <https://doi.org/10.1029/2022GC010544>

Received 26 MAY 2022

Accepted 25 AUG 2022

## Textures Induced by the Coesite-Stishovite Transition and Implications for the Visibility of the X-Discontinuity

Matthias Krug<sup>1</sup> , Morvarid Saki<sup>2</sup>, Estelle Ledoux<sup>3,4</sup> , Jeffrey P. Gay<sup>3</sup> , Julien Chantel<sup>3</sup> , Anna Pakhomova<sup>5,6</sup> , Rachel Husband<sup>5</sup> , Arno Rohrbach<sup>1</sup> , Stephan Klemme<sup>1</sup> , Christine Thomas<sup>2</sup> , Sébastien Merkel<sup>3</sup> , and Carmen Sanchez-Valle<sup>1</sup> 

<sup>1</sup>Institute for Mineralogy, University of Münster, Münster, Germany, <sup>2</sup>Institute for Geophysics, University of Münster, Münster, Germany, <sup>3</sup>CNRS, INRAE, Centrale Lille, UMR 8207 - UMET - Unité Matériaux et Transformations, University of Lille, Lille, France, <sup>4</sup>Now at Department of Geology and Geophysics, University of Utah, Salt Lake City, UT, USA, <sup>5</sup>Deutsches Elektronen-Synchrotron (DESY), Hamburg, Germany, <sup>6</sup>Now at European Synchrotron Radiation Facility, Grenoble, France

**Abstract** The coesite-stishovite phase transition is considered the most plausible candidate to explain the X-discontinuity observed at around 300 km depth in a variety of tectonic settings. Here, we investigate the microstructure in SiO<sub>2</sub> across the coesite-stishovite transition in uniaxial compression experiments. We apply the multigrain crystallography technique (MGC) in a laser-heated diamond-anvil cell (LH-DAC) to identify the seismic signature of the transition and the amount of SiO<sub>2</sub> in the mantle. While coesite displays weak lattice-preferred orientations (LPO) before the transition, stishovite develops strong LPO characterized by the alignment of [112] axes parallel to the compression direction. However, LPO has little effect on the impedance contrast across the transition, which is up to 8.8% for S-waves in a mid-ocean ridge basalt (MORB) composition at 300 km depth along a normal mantle geotherm, 10 GPa–1700 K. Therefore, 10–50 vol.% of a MORB component, corresponding to 0.6–3.2 vol.% SiO<sub>2</sub>, mechanically mixed with the pyrolytic mantle would be required to explain the range of impedance (and velocity) contrasts observed for the X-discontinuity. Based on the reflection coefficients computed for the coesite-stishovite transition, we show that the incidence angle or epicentral distance is critical for the detection of silica-containing lithologies in the upper mantle, with highest detection probabilities for small incidence angles. The intermittent visibility of the X-discontinuity may thus be explained by the seismic detectability of the coesite-stishovite transition rather than by absence of the transition or chemical heterogeneities in some specific tectonic settings.

**Plain Language Summary** Seismic studies report widespread occurrence of velocity anomalies at ~300 km depth, whose origin is still not well understood. Here, we performed experiments to check whether a phase transition in SiO<sub>2</sub> silica can explain these observations and the reasons for their widespread but not global occurrence. We reproduced the pressure and temperature conditions at 300 km depth in the laboratory and applied an advanced X-ray diffraction technique to monitor changes in the orientation of grains (i.e., microstructure) in the sample across the transition. We observe that the randomly oriented grains in the low-pressure phase display strong preferred orientation after the transition. Further, we computed the effect of grain orientations on the propagation of seismic waves and the velocity changes across the phase transitions. We conclude that 10–50 vol.% of crustal rocks embedded in the mantle are needed to explain the observed anomalies. Moreover, we compute seismic parameters associated to the phase transition to guide future exploration of mantle structures. We propose that the intermittent observation of this anomaly is related to the seismic sampling strategy rather than to lack of silica anomalies (and hence the absence of the transition) in some specific mantle settings.

## 1. Introduction

The X-discontinuity, also known as the “300 km discontinuity,” is a recurrent feature in the upper mantle at 250–350 km depth that has been extensively investigated in the past (e.g., Deuss & Woodhouse, 2002; Pugh et al., 2021; Revenaugh & Jordan, 1991; Williams & Revenaugh, 2005 and references therein). The discontinuity is seismically detected by an impedance contrast of 3%–8% in both P- and S-waves (e.g., Bagley & Revenaugh, 2008) and while it does not seem to be a global feature, its occurrence is widespread. Detections have been reported beneath continents (Hales et al., 1980; Leven, 1985; A. Li et al., 2002; Wajeman, 1988;

© 2022. The Authors.

This is an open access article under the terms of the [Creative Commons Attribution License](https://creativecommons.org/licenses/by/4.0/), which permits use, distribution and reproduction in any medium, provided the original work is properly cited.

Xu et al., 1998), in the vicinity of subduction zones (An et al., 2007; Revenaugh & Jordan, 1991; Z. Zhang & Lay, 1993), and even beneath hotspots (Courtier et al., 2007; Kemp et al., 2019).

Since it was first reported, the origin of the X-discontinuity has been a topic of debate. Because most studies reveal a rather sharp seismic contrast, that is, an impedance jump within <5 km of depth, it is argued that the origin is mineralogical rather than thermal (Schmerr et al., 2013). However, the variability in depth and occurrence in different geological settings make it difficult to narrow down possible mineralogical explanations. Hypotheses for a mineralogical origin of the X-discontinuity include: (a) the formation of hydrous phase A (Revenaugh & Jordan, 1991), (b) the orthopyroxene to high-P clinopyroxene phase transition (Woodland, 1998), (c) the coesite to stishovite phase transition (Williams & Revenaugh, 2005), (d) the formation of anhydrous phase B (Ganguly & Frost, 2006), (e) transformations involving hydrated phases in the mantle (Jacobsen et al., 2010; Mookherjee et al., 2015; Revenaugh & Jordan, 1991), and (f) the onset of partial melting (Dasgupta et al., 2013; Deuss & Woodhouse, 2002).

Among these plausible explanations, the association of the X-discontinuity to the coesite to stishovite phase transition is often preferred due to the appropriate match between the transition pressure along a normal mantle geotherm (Ono et al., 2017) and the consistent depth of the observed discontinuity (Schmerr, 2015; Schmerr et al., 2013; Williams & Revenaugh, 2005). Moreover, the coesite to stishovite transition induces a substantial increase in acoustic velocities: ~5–10 vol.% of free silica (corresponding to 4–8 wt.%, assuming a basaltic phase assemblage) is sufficient to explain the observed seismic velocities and impedance contrasts across the discontinuity (Chen et al., 2015). Free silica is not known to be present in the mantle (Irifune, 1987) but could exist both in subducted basaltic crust and in delaminated continental crust. Although questions remain whether it could explain the observed seismic features (Irifune et al., 1986; Knapp et al., 2015), subducted basaltic crust has been shown to form significant amounts of free silica at pressures relevant for the X-discontinuity both in thermodynamic calculations (Ghent et al., 2004) and experiments (Aoki & Takahashi, 2004). Delaminated continental crust, also, has been shown to contain up to ~25 vol.% of free silica (Dobrzhinetskaya & Green, 2007; Wu et al., 2009), which is hence sufficient to explain the detection of the X-discontinuity beneath continents.

Previous studies largely focused on constraining the velocity and impedance contrast across the coesite-stishovite transition from laboratory sound velocity measurements (Chen et al., 2015, 2017). Nevertheless, the subduction of oceanic plates into the mantle is known to generate complex strain patterns in the slab (Čížková et al., 2007; McNamara et al., 2001, 2003; Nippres et al., 2004), which might induce lattice-preferred orientations (LPO), also known as texture, in the stable mineral components (Long & Becker, 2010; Mainprice, 2009). To the best of our knowledge, the LPO in coesite and/or stishovite at the conditions relevant for the X-discontinuity has not yet been investigated. Distinct LPO in either of the phases could, however, generate distinct anisotropy patterns that would be a selective diagnostic feature for the seismic detection of the mineralogical transition in the mantle.

In this study, we address this issue with an in-situ study of LPO in silica across the coesite-stishovite transformation at mantle conditions by applying a novel X-ray diffraction technique based on multigrain crystallography (MGC) analysis in a laser-heated diamond-anvil cell (LH-DAC). The MGC technique, also known as 3-dimensional X-ray diffraction (3D-XRD), provides information on the microstructural properties of the sample, including the grain size and grain orientation of individual grains in a polycrystalline aggregate (Langrand et al., 2017; Sørensen et al., 2012). We apply the results to evaluate the effect of textures on the impedance contrast across the coesite-stishovite transition and further identify the seismic signature of the transition. Finally, we discuss the implications of our work for the intermittent visibility of the X-discontinuity.

## 2. Materials and Methods

### 2.1. Sample Preparation

We employed sintered polycrystalline quartz samples as starting material. High purity single-crystals of quartz were thoroughly ground in ethanol to a grain size of ~1–4 μm, dried and mixed with 10 wt% platinum powder to enable laser-coupling during the experiment. Homogenization was achieved by further mixing in ethanol. The powders were then sealed in a platinum capsule and sintered in a piston-cylinder apparatus at 1 GPa and 1473 K for 1 hr to reduce the porosity of the polycrystalline aggregate. The sintered material was then double-side polished to slabs of ~15 μm thickness using SiC abrasives and laser-cut into disks of ~20 μm diameter for the experiments.

Short-piston symmetric diamond-anvil cells equipped with Boehler-Almax diamonds (Boehler & De Hantsetters, 2004) of 250  $\mu\text{m}$  diameter culet were employed to ensure a rotation range  $\Delta\omega$  of  $60^\circ$  for the MGC data collection. Rhenium foils pre-indented to a thickness of  $\sim 30\ \mu\text{m}$  and laser-drilled with a hole of  $\sim 70\ \mu\text{m}$  diameter served as sample chambers. Disks of the sintered quartz-platinum mixtures were loaded between layers of KCl that served both as thermal insulation for the laser heating and as pressure calibrant. Pressure was determined from the equation of state of KCl as calibrated by Tateno et al. (2019).

## 2.2. MGC Experiment and Analysis

Experiments were performed at the Extreme Conditions beamline P02.2 at PETRA III (DESY, Hamburg, Germany). The X-ray beam was monochromatic, with a wavelength of  $0.2891\ \text{\AA}$  and focused down to  $1.4 \times 1.9\ \mu\text{m}$  ( $V \times H$  FWHM). We used a Perkin-Elmer XRD 1621 flat panel detector with  $2,048 \times 2,048$  pixels and a  $0.2 \times 0.2\ \text{mm}$  pixel size. The sample-detector distance, beam center and the detector tilt were calibrated using a  $\text{CeO}_2$  standard powder. Double-sided laser heating using the installed Yb-fiber laser at the beamline was performed in order to achieve high temperatures (Bykova et al., 2019; Liermann et al., 2015). The temperature was determined by spectroradiometry and monitored throughout the heating process. Uncertainties in temperature were below  $\pm 100\ \text{K}$  (Bykova et al., 2019).

The experimental sequence is schematically described in Figure 1. Coesite was first synthesized in-situ in the DAC by compressing the sintered quartz-Pt sample to 4.3 GPa at room temperature and then laser-heating for a few

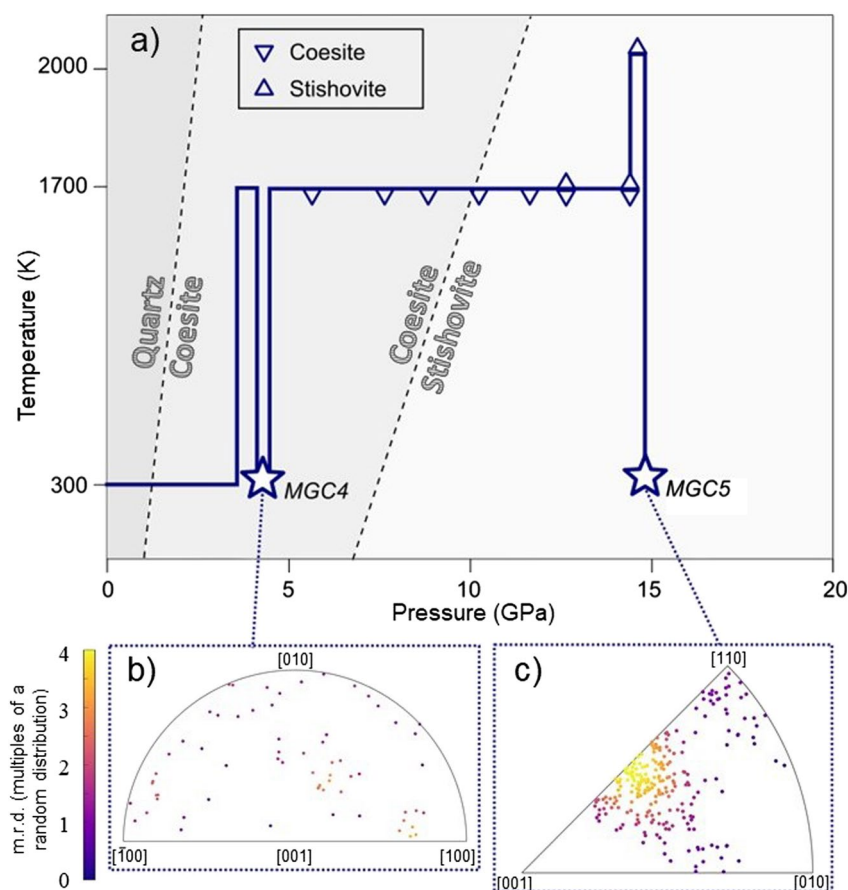


**Figure 1.** (a) Experimental pathway across the coesite-stishovite transition. Stars mark the  $P$ - $T$  conditions of the multigrain crystallography (MGC) data collection in coesite (4.3 GPa, MGC4) and stishovite (14.7 GPa, MGC5). Gray shaded areas show the theoretical stability fields of quartz, coesite and stishovite based on Bose and Ganguly (1995) and Ono et al. (2017). (b and c) Inverse pole figures of the compression direction representing the orientation of the indexed grains. Colored points mark the orientation of individual grains and the color scale is fitted to the ODF intensity at this orientation, expressed in multiples of random distribution (m.r.d.).

minutes to 1650 K. The progress of the quartz-coesite transformation was monitored by X-ray diffraction and the Dioptas software (Prescher & Prakapenka, 2015) to follow the powder diffraction reflections. The laser-heating continued until the vanishing of reflections from quartz in the diffraction pattern confirmed the complete transformation of the sample into coesite. The sample was quenched to room temperature within seconds by turning off the power of the lasers. In the next step, the sample was heated to 1700 K and compressed beyond the theoretical coesite-stishovite transformation pressure of  $\sim 10$  GPa (Ono et al., 2017), while maintaining the temperature between 1600 and 1800 K, consistent with a standard mantle geotherm (e.g., Ono, 2008). Above 12.7 GPa, the onset of the coesite-stishovite transformation was observed by the appearance of new reflections that were assigned to stishovite (Figure S1 in Supporting Information S1). Pressure was increased further to 14.7 GPa and temperature was increased up to 2000 K in steps of  $\sim 100$  K to ensure the complete transformation of the sample into stishovite after which we quenched the sample to ambient temperature. Although this temperature is larger than that of a normal mantle geotherm, we do not expect a significant effect of heating from 1700 to 2000 K on the stishovite microstructure, as this temperature range is well below the melting temperatures of both coesite and stishovite, which are on the order of  $\sim 3000$  K at  $\sim 10$  GPa (Andrault et al., 2020; Shen & Lazor, 1995).

MGC analyses were conducted after the quartz-coesite transformation at 4.3 GPa (MGC4) and after the coesite-stishovite transformation at 14.7 GPa (MGC5), at ambient temperature with the laser switched off (Figure 1). The diamond-anvil cell was rotated over  $\Delta\omega = 54^\circ$  and diffraction patterns were acquired during every  $0.5^\circ$  increment of rotation  $\delta\omega$ , with collection times of 1 s per image. This results in a series of 108 images per MGC analysis.

We provide, here, a short description of the MGC data analysis procedure. Details can be found in Langrand et al. (2017). We used the open-source software package FABLE-3DXRD (<https://github.com/FABLE-3DXRD>) complemented with our custom scripts from the TIMEleSS-MGC-tools (<https://github.com/FABLE-3DXRD/TIMEleSS>). After a thorough quality check of the images and subtraction of the background of each image, we extract a list of the locations of the observed single-grain reflections using the Peaksearch algorithm (Sørensen et al., 2012). In parallel, we compute an average of the image series, from which we obtained the lattice parameters of the relevant phases using the software MAUD (Lutterotti et al., 1997, 2014). The ImageD11 software (Wright, 2005) is then used to generate a list of potential G-vectors using the list of observed single-grain reflections and the determined lattice parameters. Each G-vector is assigned to its observed intensity and location in orientation space ( $2\theta$ ,  $\eta$  and  $\omega$  angles) and potential  $h$ ,  $k$ , and  $l$  Miller indices. The assignment of the G-vectors to sample grains is then performed using the GrainSpotter algorithm (Schmidt, 2014). Lastly, a secondary refinement is performed using FitAllB (Oddershede et al., 2010) to provide a list of better-defined sample grains. Finally, we use MTEX (Mainprice, Bachmann, Hielscher, & Schaebe, 2015; Mainprice, Bachmann, Hielscher, Schaebe, & Lloyd, 2015) in order to fit an orientation distribution function (ODF) to the list of single-grain orientations and plot the results as pole figures. Estimated errors in the grain orientations are typically below  $0.4^\circ$  in simulated datasets (Langrand et al., 2017) and they are not expected to exceed  $1\text{--}2^\circ$  for real data here.

### 2.3. Calculation of Seismic Observables

Seismic velocity and impedance contrasts for a pure  $\text{SiO}_2$  system and for a MORB assembly across the coesite-stishovite transition are reported in Table 2. The velocity contrast is defined as

$$\Delta V = \frac{2(V_b - V_a)}{V_b + V_a} \quad (1)$$

where  $V_a$  and  $V_b$  are the velocities above and below the discontinuity, respectively. Similarly, the impedance contrast is defined as

$$\Delta Z = \frac{2(Z_b - Z_a)}{Z_b + Z_a} \quad (2)$$

where  $Z_a$  and  $Z_b$  are defined as the impedances above and below the discontinuity, respectively. The calculations were performed at 10 GPa and 1700 K, corresponding to the location of the transition along a normal mantle geotherm (Ono et al., 2017) and for two case scenarios: (a) isotropic elastic behavior of all phases in both the pre- and post-transition assemblies and (b) isotropic behavior of all phases in the pre-transition assembly and textured stishovite in the post-transition assembly (Table 2). We first extrapolated data for the density and the

**Table 1**  
*Multigrain Crystallography (MGC) Indexing Statistics*

	P/GPa	Silica phase	No. of G-vectors	% G-vectors assigned	Total no. of grains	No. of high-quality grains
MGC4	4.3	Coesite	3,916	88	111	64
MGC5	14.7	Stishovite	3,455	85	365	240

*Note.* For each indexing, the table shows the total number of G-vectors extracted from the diffraction images, the proportion of G-vectors assigned to silica grains, the number of silica grains after GrainSpotter indexing and the number of high-quality indexed grains after the second-stage refinement with FitAllB.

elastic moduli of isotropic aggregates of coesite, garnet and clinopyroxene to 10 GPa and 1700 K using the finite strain formalism (Chantel et al., 2016; Davies & Dzierwinski, 1975; Table S1 in Supporting Information S1). In addition, we also account for effects of texture on the elastic properties of stishovite (Figure 1). We use the single-crystal elastic tensor  $C_{ij}$  of stishovite at 10 GPa and 1700 K based on high-pressure Brillouin scattering data (Jiang et al., 2009) and a temperature correction derived from molecular dynamics simulations of Yang and Wu (2014). The effect of texture is modeled using our experimental ODF and the MTEX software (Mainprice, Bachmann, Hielscher, & Schaeben, 2015; Mainprice, Bachmann, Hielscher, Schaeben, & Lloyd, 2015). The  $C_{ij}$  tensors for both single-crystal and textured polycrystalline stishovite at 10 GPa and 1700 K are reported in Table S2 of Supporting Information S1.

We computed the aggregate properties of both textured stishovite and the coesite- and stishovite-bearing MORB assemblies from the individual elastic  $C_{ij}$  using a Voigt-Reuss-Hill (VRH) average (Watt et al., 1976). The effect of texture in garnet, the dominant phase in MORB, on the seismic properties of the assembly is expected to be negligible as garnet's anisotropy cannot be resolved at relevant mantle pressures (Conrad et al., 1999; Jiang et al., 2004). Clinopyroxene, on the other hand, can display strong and distinct LPO (Q. Wang et al., 2009), which may be also relevant for the pressure conditions of the X-discontinuity (Hao et al., 2021). However, in order to isolate the seismic signature of the coesite-stishovite phase transition, isotropic behavior was assumed for both garnet and clinopyroxene in the MORB assembly before and after the transition. Modal proportions of the pre-transition MORB assembly were 52.8 vol.% garnet, 40.3 vol.% clinopyroxene and 6.9 vol.% coesite (after Aoki & Takahashi, 2004); modal proportions of the post-transition MORB assembly were 60.9 vol.% garnet, 33.1 vol.% clinopyroxene, and 6.0 vol.% stishovite (Aoki & Takahashi, 2004).

### 3. Results

#### 3.1. MGC and Experimental LPO

Table 1 shows the number of G-vectors and the number of grains that were obtained from the MGC4 and MGC5 analyses. We extract 3916 and 3455 G-vectors for coesite and stishovite, respectively. GrainSpotter then assigns those G-vectors to 111 and 365 grains of coesite and stishovite, respectively, indexing between 85% and 88% of all G-vectors. The different number of grains between both phases despite a similar number of G-vectors can be explained by the different crystal structures, as the monoclinic coesite produces more reflections than the tetragonal stishovite due to its lower symmetry. This increase in the number of grains as coesite transforms to stishovite is related to the reconstructive nature of the transformation in which nuclei of stishovite grow inside the coesite matrix.

Figure 1 shows the orientations of the coesite and stishovite grains at 4.3 and 14.7 GPa, respectively. Coesite displays a weak LPO with a maximum intensity of 2.0 m.r.d. (multiples of a random distribution) and several maxima (Figure 1b). This observation is in agreement with the results of previous studies, which showed only weak LPO induced by the quartz-coesite transformation, both in axial compression experiments and natural samples (J. F. Zhang et al., 2013). After the phase transition to stishovite, however, the maximum texture intensity increases to 4.0 m.r.d., and we observe a clear LPO dominated by the alignment of the [112] axes of stishovite crystals parallel to compression direction (Figure 1c).

#### 3.2. Seismic Signature of the Coesite-Stishovite Transformation

The calculated seismic velocity contrasts between isotropic coesite and stishovite at 10 GPa and 1700 K, 40.5% for P-waves and 63.7% for S-waves, translate into a large impedance contrast of 69.3% and 90.2% for P- and S-waves respectively (Table 2). The shear impedance contrast is significantly larger than the 75% reported by Chen et al. (2017), a value that is based on direct sound velocity measurements in polycrystalline coesite and stishovite at high pressures up to 1273 K by ultrasonic interferometry (Chen et al., 2015, 2017; B. Li et al., 1996). Increasing temperature decreases the impedance contrast (Chen et al., 2015, 2017). The difference between our

**Table 2**

*Calculated Velocity Contrasts  $\Delta V$  and Impedance Contrasts  $\Delta Z$  for Both P-Waves and for the Fast ( $V_{S1}$ ) and Slow ( $V_{S2}$ ) Polarizations of the S-Waves Across the Coesite to Stishovite Transition at 10 GPa and 1700 K*

	Pure SiO <sub>2</sub> system			MORB		
	Isotropic coesite/ isotropic stishovite	Isotropic coesite/ textured stishovite (min)	Isotropic coesite/ textured stishovite (max)	Isotropic coe/ isotropic St	Isotropic coe/ textured St (min)	Isotropic coe/textured St (max)
$\Delta V_P$ (%)	40.50	39.15	44.28	3.53	3.49	3.66
$\Delta V_{S1}$ (%)	63.69	62.97	67.34	5.38	5.53	5.88
$\Delta V_{S2}$ (%)	$=\Delta V_{S1}$	59.59	63.48	$=\Delta V_{S1}$	5.24	5.59
$\Delta Z_P$ (%)	69.29	68.05	72.75	6.42	6.37	6.54
$\Delta Z_{S1}$ (%)	90.20	89.57	93.44	8.26	8.41	8.76
$\Delta Z_{S2}$ (%)	$=\Delta Z_{S1}$	86.56	90.02	$=\Delta Z_{S1}$	8.12	8.48

*Note.* Results are provided in pure silica and in MORB. Ranges for velocity and impedance contrasts in textured stishovite and stishovite-bearing MORB are given as minimum and maximum values.

results and those of Chen et al. (2017) could arise from the temperature corrections applied here to the stishovite elasticity data, the intrinsic limitations of averaging schemes to constrain the shear elastic properties of polycrystalline aggregates of anisotropic phases (Watt et al., 1976), as well as from possible effects of microstructures and porosity in the samples that could affect the results of ultrasonic studies (Chen et al., 2015, 2017). Nevertheless, our calculations confirm that the impedance contrast between pure coesite and stishovite is large. The transition could hence potentially be detected using seismic observation with a relatively low proportion of free silica in the Earth's mantle.

Accounting for the effect of other phases, the impedance contrast of elastically isotropic SiO<sub>2</sub>-bearing MORB assemblies yields 6.4% and 8.3% for the P- and S-wave, respectively (Table 2). The addition of the effect of LPO in stishovite in MORB changes the impedance contrast for P- and S-waves by up to 0.12% and 0.51%, respectively. The effect of microstructure on impedance contrast is hence significantly lower than that of other parameters, such as density and seismic velocities (Table 2).

The presence of textured stishovite would cause seismic anisotropy in the assembly. Figure 2 displays the projections of the S-wave anisotropy of both single-crystal and textured polycrystalline stishovite calculated at 10 GPa and 1700 K using the  $C_{ij}$  tensors of Table S2 in Supporting Information S1. While a stishovite single-crystal can yield a shear wave anisotropy of up to 37% (Figure 2a), textured polycrystalline stishovite as in our experiment yields a maximum shear anisotropy of 6.8%, for S-waves traveling  $\sim 45^\circ$  off the compression axis (Figure 2b). The shear wave anisotropy decreases down to 0.40% for a stishovite-bearing MORB assemblage, however, and would be even further reduced as MORB is mixed within the pyrolytic mantle (Figure 2c), suggesting that anisotropy from stishovite will be difficult to detect seismically.

## 4. Discussion

### 4.1. Evolution of LPO Across the Coesite to Stishovite Transition

The MGC analysis of coesite results in a total of 111 grains, or 64 grains after second-stage refinement (Table 1). A low number of grains can lead to an overestimation of the ODF intensity as local maxima tend to appear stronger than they would be in a sample with similar orientation distribution but a higher number of grains. Thus, we interpret the weak local maxima observed in the ODF of coesite as a random orientation distribution rather than as a significant LPO. Because the MGC analysis of coesite was performed directly after the transformation from quartz, the random orientation of the crystals is consistent with the reconstructive nature of the quartz-coesite transformation that should not induce any inherited LPO in the daughter crystals (Tolédano & Dmitriev, 1996). Recent studies have shown that in rare cases, such as during impacts, a crystallographic parent-daughter relation can be preserved throughout the quartz-coesite transition (Campanale et al., 2019; Glass et al., 2020; Masotta et al., 2020). However, the exact conditions required for such coherent orientation relationships, as well as the

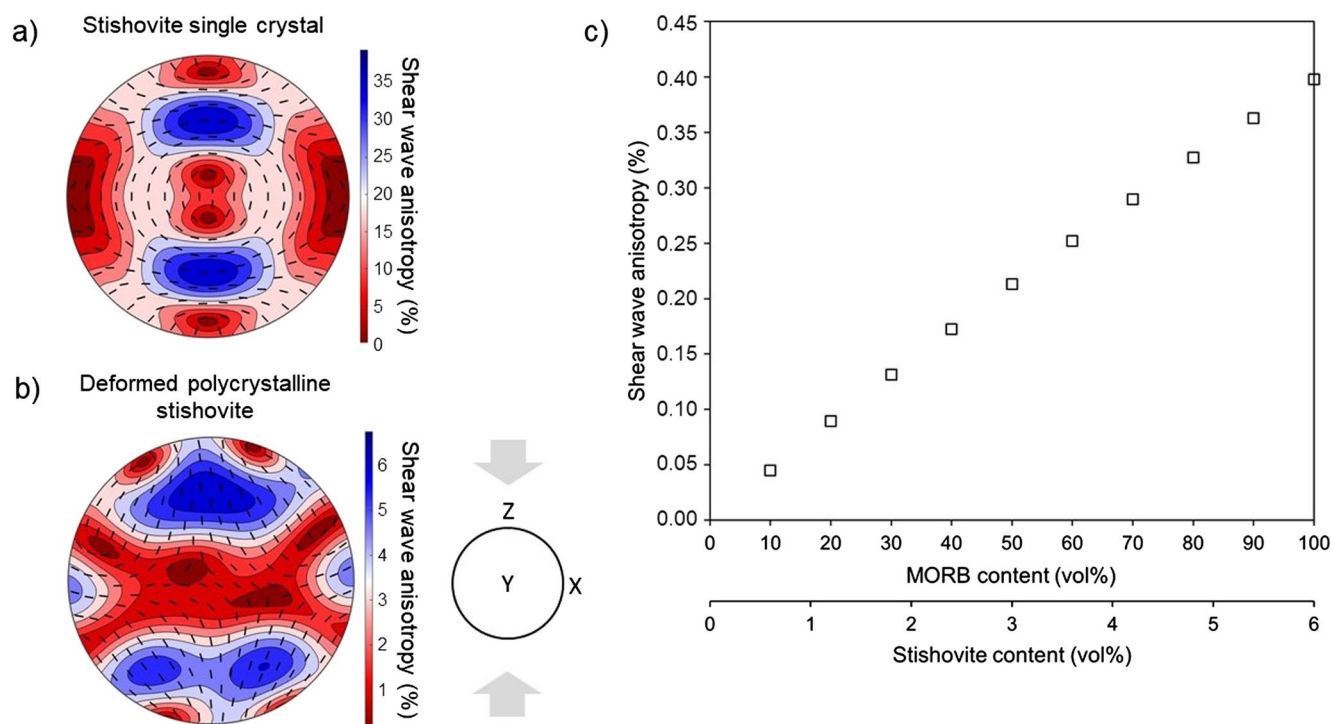


**Figure 2.** Projections of S-wave anisotropy (in %) of (a) single-crystal stishovite and (b) deformed polycrystalline stishovite at 10 GPa and 1700 K. Black lines mark the polarization of the fast shear wave, that is,  $V_{S1}$ . Compression for both single crystal and polycrystalline stishovite is parallel to the z-axis and shown in the small inset. (c) Maximum shear wave anisotropy expected for a mechanical mixture of MORB and pyrolite as a function of MORB (and textured stishovite, in vol%) content.

corresponding transformation mechanism, remain unclear. They are likely not comparable with the experiments conducted in this study, nor with the conditions of the Earth's mantle.

After transformation we index 365 oriented stishovite grains. The presence of LPO after the transition from coesite is counterintuitive as one would expect a reconstructive transformation between coesite and stishovite and, hence, a random nucleation. Plausible explanations for this observation include residual stresses in the compression chamber, despite the presence of a pressure medium and the elevated temperatures, and/or that the transformation proceeds through a martensitic-like mechanism as observed for rare occurrences of the quartz-coesite transformation (Campanale et al., 2019). Yet, the experimental evidence for a martensitic-like mechanism in the coesite-stishovite transition has not been reported.

The limited number of MGC analyses does not allow us to decide whether coesite could develop a significant LPO upon compression to the transition pressure. A previous experimental study of the deformation behavior of coesite, conducted only at lower temperatures, was not conclusive (Renner et al., 2001). Natural coesite from impact sites display LPO (Fazio et al., 2017; Langenhorst & Deutsch, 2012). Yet they are difficult to compare with the present study due to differences in the formation mechanism. Slowly deformed natural coesite, as found in some ultra-high pressure metamorphic rocks, usually occurs only as few inclusions of individual crystals (e.g., Butler et al., 2013; Massonne, 2001; X. Wang et al., 1989) that are not sufficient to deduce LPO information. Because of the limited knowledge and ambiguous results of previous studies about coesite deformation behavior and coesite LPO, we think it is more likely to assume the development of a less pronounced and weak LPO in coesite rather than a significant strong one.

Under the assumption that stishovite grains formed with random orientation, it is possible that the strong LPO observed here could have developed in response to the over-compression of the sample from 12.7 GPa, when stishovite is first detected (Figure 1), to 14.7 GPa, when the transformation is completed. However, based on the experimental results of Kaercher et al. (2015), we consider it unlikely that a compression of only 2 GPa is sufficient to generate strong LPO in stishovite. We, therefore, assume that the LPO observed in stishovite arises from the nucleation of grains in the presence of residual stress in the compression chamber. Although the residual

stress is difficult to evaluate in our experiment, based on stress measurements during stishovite deformation in previous diamond-anvil cells and multi-anvil experiments (Hunt et al., 2019; Nisr et al., 2014), we estimate the residual stress in our experiment to be on the order of  $1 \pm 1$  GPa. These stress conditions are of the same order of magnitude as those estimated for subduction zones by 2D thermo-mechanical simulations, that is, several hundreds of MPa (Bessat et al., 2020). A direct application of these results to natural systems would, however, require more precise stress measurements during the experiments. The appearance of LPO following a reconstructive phase transformation has previously been documented in other materials, such as in  $\text{MgSiO}_3$  bridgmanite (Miyagi & Wenk, 2016). This is, to the best of our knowledge, the first observation in silica polymorphs.

Interestingly, our LPO in stishovite differs from previous results. To our knowledge, transformation textures were only reported when stishovite is formed from quartz in the laser-heated diamond-anvil cell, with a strong maximum with the [001] axis parallel to compression (Kaercher et al., 2015). Deformation of stishovite in compression at ambient temperature seems to strengthen the [001] texture (Kaercher et al., 2015; Nisr et al., 2014) whereas TEM observations of stishovite deformed at 14 GPa and 1573 K report [001] dislocations in either {110}, {100}, or {210} slip planes (Cordier et al., 2004; Texier & Cordier, 2006) and deformation of polycrystalline stishovite at 12 GPa and 1873–2073 K reports textures consistent with glide in [001] in either {110} or {100} (Xu et al., 2020). The [112] compression texture we report here is hence not consistent with these previous works, although a direct comparison between the different studies is not straightforward. The effect of the Pt embedded in the sample on the observed textures cannot be constrained at this point and might not be excluded as a potential source of differences. We note, however, that the present study addresses LPO formed in stishovite right after the transformation from coesite with minimal further deformation. The transformation process itself could be accompanied by the development of unusual stress patterns that results in the directional growth of stishovite crystals and hence textures that are not produced as a result of deformation. These observations thus highlight the role of the starting material,  $P/T$  path and stress patterns on the generation of textures in stishovite.

#### 4.2. Impedance Contrast of the X-Discontinuity

The microstructures and texturing behavior identified in our study, that is, weak LPO in coesite and strong LPO in stishovite (Figure 1), may provide valuable constraints on the seismic signature of the coesite-stishovite transition in the upper mantle. Figure 3 shows the results of a worldwide compilation of shear seismic impedance contrasts and depths for the X-discontinuity reported by Schmerr (2015). In order to constrain the MORB fraction required to match the observations, we computed the pressure and composition dependence of the shear impedance contrast associated to the coesite-stishovite transition (Figure 3) with MTEX (Mainprice, Bachmann, Hielscher, & Schaeben, 2015; Mainprice, Bachmann, Hielscher, Schaeben, & Lloyd, 2015).

Our calculations show that depth (or pressure) has a rather negligible effect on the shear impedance contrast, while the MORB fraction is the dominant parameter (Figure 3). We find that a pure and undeformed MORB assemblage would produce a shear impedance contrast of around 8% (Table 2), which is significantly higher than the 2%–5% reported by Williams and Revenaugh (2005). Note, however, that these early estimates were conducted based on poorly constrained high temperature extrapolations of the shear properties of stishovite by assuming constant Poisson's ratios. Our calculations, using most recent high pressure-high temperature elasticity data for coesite and stishovite and the experimental textures derived here, yield a maximum shear impedance contrast of about 8.8% (Table 2).

Based on the results shown in Figure 3, we estimate that MORB contents of 10–50 vol.% would be required to produce shear impedance contrasts that match the seismic observations. This range of MORB fractions is lower than the 60–70 vol.% estimated by Kemp et al. (2019), which was used to explain the seismic observations underneath Hawaii. However, the calculations by Kemp et al. (2019) do not warrant a direct comparison with our estimates, as they were performed using harzburgite-basalt mixtures and, moreover, the authors derived the basalt fraction from intensity ratios of stacked receiver functions rather than from the impedance contrasts. Nevertheless, both studies support the idea that the X-discontinuity could be explained by the coesite to stishovite transition. Our calculations also indicate that MORB-enriched domains with MORB fractions of up to 50 vol.% are required to match the observations. The observation of the X-discontinuity and its relation to the coesite-stishovite transformation hence implies that subducted basaltic material can persist relatively unmixed in the average mantle.

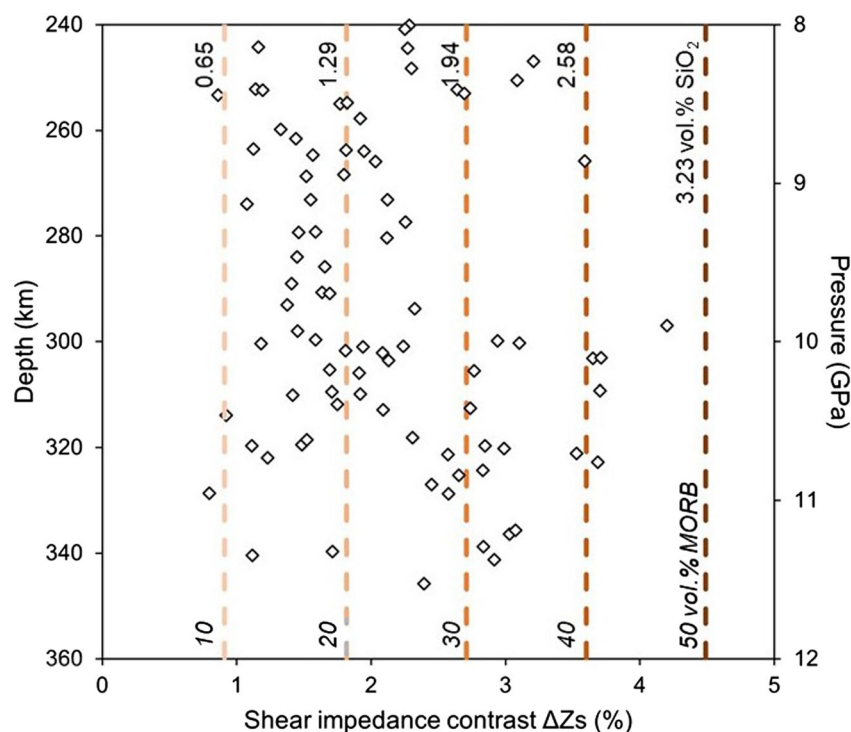


**Figure 3.** Calculated shear impedance contrasts  $\Delta Z_s$  due to the coesite-stishovite transformation versus depth, composition and seismic observations. For the calculations, we assumed no texture for coesite and the texture determined in MGC5 for stishovite. Vertical dotted lines are  $\Delta Z_s$  values for mechanical mixtures of 10, 20, 30, 40, and 50 vol.% MORB and pyrolite (vertical numbers in italics) at pressures ranging from 8 to 12 GPa. Respective free silica content is given based on the assumption of 6.45 vol.% free silica in MORB (vertical numbers in non-italics), reported by Aoki and Takahashi (2004). Diamonds are the impedance contrasts of 86 observations of the X-discontinuity between 250 and 350 km depth reported in Schmerr (2015) with a depth uncertainty <5 km.

### 4.3. Implications for the Visibility of the X-Discontinuity

The X-discontinuity is not detected globally. Hence, the question remains whether this is due (a) to a lack of free silica in the mantle in specific settings or (b) to the probing geometry of seismic studies. To investigate this question, we evaluate the seismic reflectivity for underside reflections of P- and S-waves at the coesite to stishovite phase transition using Zoeppritz's equations (Zoeppritz, 1919) for both pure silica and for a MORB assemblage (Figure 4). We modeled two scenarios, one with no LPO and one with a textured stishovite in the lower layer using the experimentally determined LPO and the same procedure as in Saki et al. (2018). This assumes a uniaxial downward compression geometry, which is relevant for a fragment of basaltic material sinking into the mantle, either by slab subduction or by crust delamination (Frohlich, 1989; Vavryčuk, 2006). Since underside reflections from deep discontinuities are compared with the surface reflected PP and SS waves, we also show the reflection coefficients of the PP and SS waves at the free surface (Figures 4e and 4f), which were calculated using wave speeds and densities reported by Meissner and Kern (2011). Especially for polarity observations (e.g., Saki et al., 2019), the comparison of precursors to the main phase reflected at the surface is essential. Comparing the different panels in Figure 4, reflection coefficients for a MORB assembly are one order of magnitude lower than those of pure silica due to the dilution of the transition effect in a multi-phase assemblage. Nevertheless, Figure 4 reveals a similar trend for the reflection coefficient versus incidence angle for both pure silica and MORB and are discussed below.

The reflection coefficient for PP waves of the coesite-to-stishovite transition shows a characteristic shape where, for incidence angles of around 50–60° the P-reflectivity reaches a minimum (close to the zero-line), indicating a small amplitude of the reflected waves for these angles of incidence. Toward smaller and larger incidence angles the reflectivity increases (albeit in the negative range) resulting in larger amplitudes of seismic waves reflecting at the boundary. For the P-wave underside reflection at the coesite-stishovite transition, the results show that

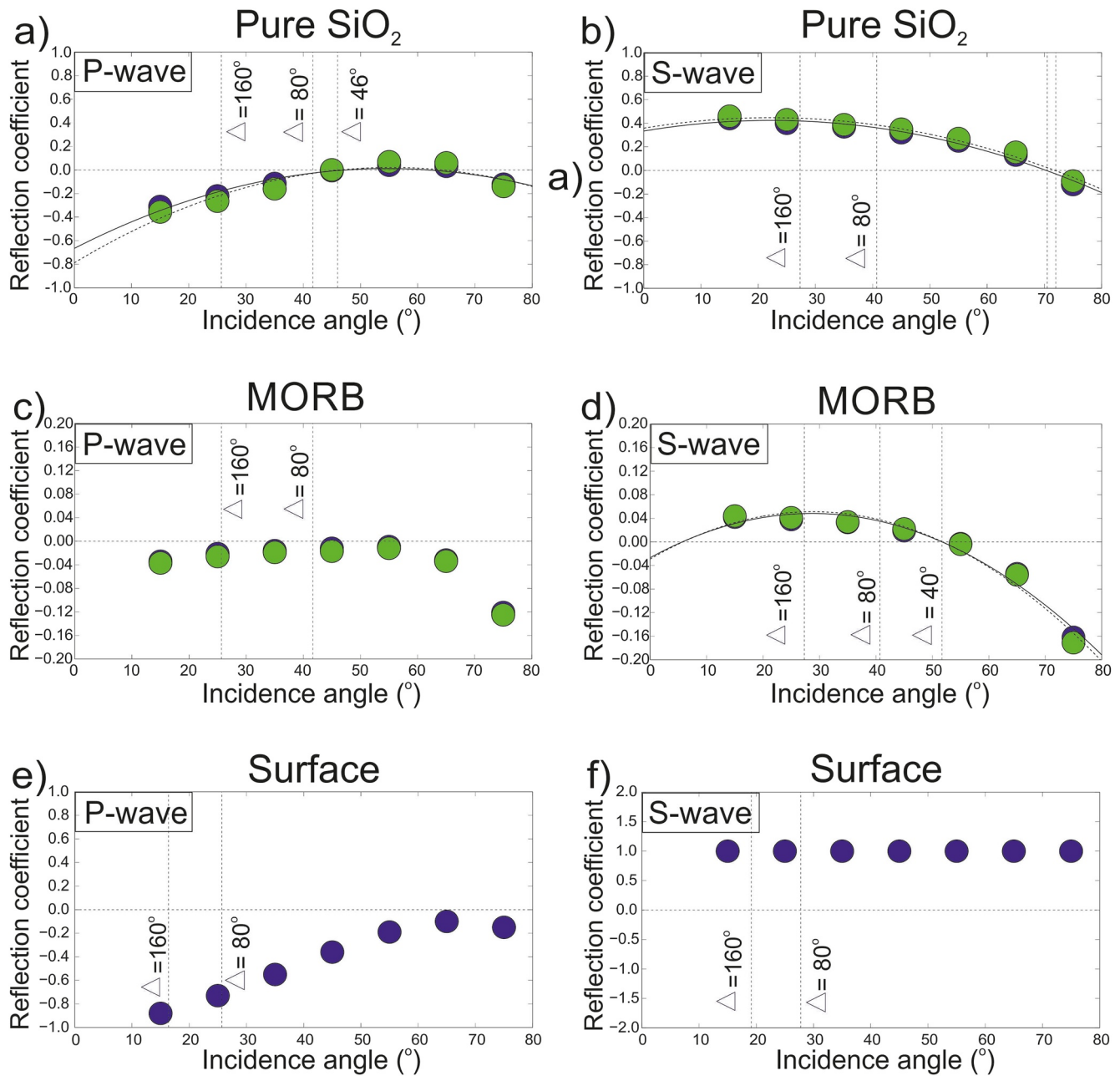


**Figure 4.** Calculated reflection coefficients for the coesite-stishovite transition (underside reflections) as a function of incidence angle for pure silica (a and b) and a MORB assemblage (c and d). PP- and SS-wave reflections off the surface are shown for comparison (e and f). Corresponding epicentral distances of 160° and 80° are marked for reference, as well as the distances of the zero-line crossing in (a and d). Note the different y-axes. Blue symbols (a–d): Randomly oriented coesite and randomly oriented stishovite. Green symbols (a–d): Randomly oriented coesite and textured stishovite. Blue symbols (e–f): PP and SS underside reflections off the surface.

the reflection coefficient of both the textured and the random stishovite cases follow this trend. For pure silica, however, the reflectivity stays near the zero-line for large incidence angles (Figure 4a), that is, for small epicentral distances, whereas it strongly increases for the MORB assemblage (Figure 4c). Comparison to the surface PP reflection (Figure 4e) indicates a similar shape of the reflection coefficient with incidence angle as pure silica (Figure 4a) and MORB (Figure 4c) but the reflection coefficient is large at the incidence angles for distances generally used for PP studies.

For the S-wave, the reflection coefficients decrease with increasing angle of incidence, except for the surface reflection (Figure 4f). A reversal in the sign of the reflection coefficient for the MORB assemblage is observed for incidence angles above  $\sim 55^\circ$ , corresponding to  $40^\circ$  epicentral distance when interpolated (Figure 4d). The reversal for pure  $\text{SiO}_2$  would eventually be reached for incidence angles over  $70^\circ$ . Note, however, that no SS underside reflections at 300 km depth exist at these distance ranges. For S-waves, differences between the results for textured stishovite and non-textured stishovite are very small and potentially not detectable.

The present results thus show the critical role of the incidence geometry on the intermittent visibility of the X-discontinuity if it is indeed associated to the coesite-stishovite transition. This contrasts with SS reflections at the surface of the Earth, with amplitudes that are independent of the incidence angle (Figure 4f), and PP reflections that never cross the zero-line (Figure 4e). The dependence of reflection coefficients with incidence angle may then help to guide future exploration of the structure of the X-discontinuity. According to our calculations, the X-discontinuity would be best detected for smaller incidence angles where the reflection coefficient is far from the zero-line, both for P- and for S-waves. In addition, the different shapes of the curves for the reflection coefficient for pure  $\text{SiO}_2$  and MORB could be indicative for the presence (and amount) of  $\text{SiO}_2$ . While the curve for pure  $\text{SiO}_2$  does not cross the zero-line, a polarity reversal for S-waves is expected at angles larger than  $55^\circ$  for MORB, similar to reflection coefficients for the olivine-wadsleyite transition at 410 km (Saki et al., 2018) as well as other SS underside reflections. The more interesting behavior lies in the P-wave reflectivity, which shows a subtle change in polarity for pure  $\text{SiO}_2$  while it stays below the zero-line in the case of the PP reflection off the surface. Although this polarity reversal can also be seen for the case of the S-wave reflectivity, this would happen only at unrealistically high incidence angles of  $>70^\circ$ .

## 5. Conclusions

Here, we show that the transformation from coesite to stishovite induces significant LPO in the daughter phase, which we associate to the presence of residual stress in the compression chamber. Although the actual stress patterns in the mantle are likely to be more complicated than those in our experiments (Čížková et al., 2007; McNamara et al., 2001, 2003; Nippres et al., 2004), it is possible that mantle stresses would cause a similar behavior in silica, that is, the development of a pronounced LPO in stishovite upon formation at  $\sim 300$  km depth. The validity of our results for stress regimes of different kinds remains to be tested in future studies to fully verify the observed effect. Complementary, theoretical investigations of the transformation mechanism between silica polymorphs may shed light on the nature and circumstances of such an LPO-inducing transformation.

We note that our results apply only to the conditions where silica is supplied to the mantle either by subduction or delamination of crustal material, as our experiments were designed to investigate the microstructures across the forward transformation, that is, from coesite to stishovite. Further investigations of the reverse transformation may be required to interpret other plausible scenarios, which involve the formation of deep eclogitic pools (DEP) by the entrainment of former subducted material by mantle plumes (Kemp et al., 2019; Rein et al., 2020).

If the X-discontinuity is indeed associated to the coesite-stishovite transformation, its detectability strongly depends on the angle of incidence of the seismic wave. In particular, we show that waves with incidence angles larger than  $40^\circ$  for P-waves and  $25^\circ$  for S-waves may overlook the discontinuity. This hence calls for a careful data selection for the investigation of the X-discontinuity in future seismic studies, as the effect of incidence angle could be a key parameter in solving the puzzle of the intermittent visibility of the X-discontinuity.

## Data Availability Statement

Diffraction patterns used for the MGC analysis are freely available in the data repository <https://uni-muenster.sciebo.de/s/y081sUCrB6qBVW3>.

## References

- Čížková, H., van Hunen, J., & van den Berg, A. (2007). Stress distribution within subducting slabs and their deformation in the transition zone. *Physics of the Earth and Planetary Interiors*, 161(3–4), 202–214. <https://doi.org/10.1016/j.pepi.2007.02.002>
- An, Y., Gu, Y. J., & Sacchi, M. D. (2007). Imaging mantle discontinuities using least squares Radon transform. *Journal of Geophysical Research*, 112(10), B10303. <https://doi.org/10.1029/2007JB005009>

## Acknowledgments

This study was financed by the bilateral ANR-DFG TIMEleSS project (ANR-17-CE31-0025; TH 1530/18-1; SA 2585/3-1; SP1216/8-1) and the bilateral PROCOPE-PPP program (PHC 40555PC; DAAD 57390184). The research leading to this result has been supported by the project CALIPSOplus under the Grant Agreement 730872 from the EU Framework Programme for Research and Innovation HORIZON 2020. We acknowledge DESY (Hamburg, Germany), a member of the Helmholtz Association HGF, for the provision of experimental facilities. Parts of this research were carried out at PETRA III. Beamtime was allocated for proposals 20180851 and 20010016. We thank the Geomuseum of the University of Münster for providing the quartz sample. MK acknowledges support from a mobility grant from the DAAD (Grant: 57504619) for a 6-month research stay at the University of Lille (France). We thank two anonymous reviewers for comments that helped to improve the manuscript and Dr. C. Faccenna for efficient editorial handling.

- Andraut, D., Morard, G., Garbarino, G., Mezouar, M., Bouhifd, M. A., & Kawamoto, T. (2020). Melting behavior of  $\text{SiO}_2$  up to 120 GPa. *Physics and Chemistry of Minerals*, 47(2), 1–9. <https://doi.org/10.1007/s00269-019-01077-3>
- Aoki, I., & Takahashi, E. (2004). Density of MORB eclogite in the upper mantle. *Physics of the Earth and Planetary Interiors*, 143(1–2), 129–143. <https://doi.org/10.1016/j.pepi.2003.10.007>
- Bagley, B., & Revenaugh, J. (2008). Upper mantle seismic shear discontinuities of the Pacific. *Journal of Geophysical Research*, 113(12), 1–9. <https://doi.org/10.1029/2008JB005692>
- Bessat, A., Duretz, T., Hetényi, G., Pilet, S., & Schmalholz, S. M. (2020). Stress and deformation mechanisms at a subduction zone: Insights from 2-D thermomechanical numerical modelling. *Geophysical Journal International*, 221(3), 1605–1625. <https://doi.org/10.1093/gji/ggaa092>
- Boehler, R., & De Hantsetters, K. (2004). New anvil designs in diamond-cells. *High Pressure Research*, 24(3), 391–396. <https://doi.org/10.1080/08957950412331323924>
- Bose, K., & Ganguly, J. (1995). Quartz-coesite transition revisited: Reversed experimental determination at 500–1200°C and retrieved thermochemical properties. *American Mineralogist*, 80(3–4), 231–238. <https://doi.org/10.2138/am-1995-3-404>
- Butler, J. P., Jamieson, R. A., Steenkamp, H. M., & Robinson, P. (2013). Discovery of coesite-eclogite from the Nordøyane UHP domain, Western Gneiss Region, Norway: Field relations, metamorphic history, and tectonic significance. *Journal of Metamorphic Geology*, 31(2), 147–163. <https://doi.org/10.1111/jmg.12004>
- Bykova, E., Aprilis, G., Bykov, M., Glazyrin, K., Wendt, M., Wenz, S., et al. (2019). Single-crystal diffractometer coupled with double-sided laser heating system at the Extreme Conditions Beamline P02.2 at PETRAIII. *Review of Scientific Instruments*, 90(7), 073907. <https://doi.org/10.1063/1.5108881>
- Campanale, F., Mugnaioli, E., Folco, L., Gemmi, M., Lee, M. R., Daly, L., & Glass, B. P. (2019). Evidence for subsolidus quartz-coesite transformation in impact ejecta from the Australasian tektite strewn field. *Geochimica et Cosmochimica Acta*, 264, 105–117. <https://doi.org/10.1016/j.gca.2019.08.014>
- Chantel, J., Manthilake, G. M., Frost, D. J., Beyer, C., Ballaran, T. B., Jing, Z., & Wang, Y. (2016). Elastic wave velocities in polycrystalline  $\text{Mg}_3\text{Al}_2\text{Si}_3\text{O}_{12}$ -pyrope garnet to 24 GPa and 1300 K. *American Mineralogist*, 101(4), 991–997. <https://doi.org/10.2138/am-2016-5335>
- Chen, T., Gwanmesia, G. D., Wang, X., Zou, Y., Liebermann, R. C., Michaut, C., & Li, B. (2015). Anomalous elastic properties of coesite at high pressure and implications for the upper mantle X-discontinuity. *Earth and Planetary Science Letters*, 412, 42–51. <https://doi.org/10.1016/j.epsl.2014.12.025>
- Chen, T., Liebermann, R. C., Zou, Y., Li, Y., Qi, X., & Li, B. (2017). Tracking silica in Earth's upper mantle using new sound velocity data for coesite to 5.8 GPa and 1073 K. *Geophysical Research Letters*, 44(15), 7757–7765. <https://doi.org/10.1002/2017GL073950>
- Conrad, P. G., Zha, C. S., Mao, H. K., & Hemley, R. J. (1999). The high-pressure, single-crystal elasticity of pyrope, grossular, and andradite. *American Mineralogist*, 84(3), 374–383. <https://doi.org/10.2138/am-1999-0321>
- Cordier, P., Mainprice, D., & Mosenfelder, J. L. (2004). Mechanical instability near the stishovite- $\text{CaCl}_2$  phase transition: Implications for crystal preferred orientations and seismic properties. *European Journal of Mineralogy*, 16(3), 387–399. <https://doi.org/10.1127/0935-1221/2004/0016-0387>
- Courtier, A. M., Bagley, B., & Revenaugh, J. (2007). Whole mantle discontinuity structure beneath Hawaii. *Geophysical Research Letters*, 34(17), 1–5. <https://doi.org/10.1029/2007GL031006>
- Dasgupta, R., Mallik, A., Tsuno, K., Withers, A. C., Hirth, G., & Hirschmann, M. M. (2013). Carbon-dioxide-rich silicate melt in the Earth's upper mantle. *Nature*, 493(7431), 211–215. <https://doi.org/10.1038/nature11731>
- Davies, G. F., & Dziewonski, A. M. (1975). Homogeneity and constitution of the Earth's lower mantle and outer core. *Physics of the Earth and Planetary Interiors*, 10(4), 336–343. [https://doi.org/10.1016/0031-9201\(75\)90060-6](https://doi.org/10.1016/0031-9201(75)90060-6)
- Deuss, A., & Woodhouse, J. H. (2002). A systematic search for mantle discontinuities using SS-precursors. *Geophysical Research Letters*, 29(8), 8–11. <https://doi.org/10.1029/2002GL014768>
- Dobrzhinetskaya, L. F., & Green, H. W. (2007). Experimental studies of mineralogical assemblages of metasedimentary rocks at Earth's mantle transition zone conditions. *Journal of Metamorphic Geology*, 25(2), 83–96. <https://doi.org/10.1111/j.1525-1314.2007.00694.x>
- Fazio, A., Mansfeld, U., & Langenhorst, F. (2017). Coesite in suevite from the Ries impact structure (Germany): From formation to postshock evolution. *Meteoritics and Planetary Science*, 52(7), 1437–1448. <https://doi.org/10.1111/maps.12849>
- Frohlich, C. (1989). The nature of deep-focus earthquakes. *Annual Review of Earth and Planetary Sciences*, 17(4), 227–254. <https://doi.org/10.1146/annurev.ea.17.050189.001303>
- Ganguly, J., & Frost, D. J. (2006). Stability of anhydrous phase B: Experimental studies and implications for phase relations in subducting slab and the X discontinuity in the mantle. *Journal of Geophysical Research*, 111(6), 1–8. <https://doi.org/10.1029/2005JB003910>
- Ghent, E. D., Dipple, G. M., & Russell, J. K. (2004). Thermodynamic models for eclogitic mantle lithosphere. *Earth and Planetary Science Letters*, 218(3–4), 451–462. [https://doi.org/10.1016/S0012-821X\(03\)00678-2](https://doi.org/10.1016/S0012-821X(03)00678-2)
- Glass, B. P., Folco, L., Masotta, M., & Campanale, F. (2020). Coesite in a Muong Nong-type tektite from Muong Phin, Laos: Description, formation, and survival. *Meteoritics and Planetary Science*, 21(2), 1–21. <https://doi.org/10.1111/maps.13433>
- Hales, A. L., Muirhead, K. J., & Rynn, J. M. W. (1980). A compressional velocity distribution for the upper mantle. *Tectonophysics*, 63(1–4), 309–348. [https://doi.org/10.1016/0040-1951\(80\)90119-5](https://doi.org/10.1016/0040-1951(80)90119-5)
- Hao, M., Zhang, J. S., Zhou, W.-Y., & Wang, Q. (2021). Seismic visibility of eclogite in the Earth's upper mantle—Implications from high pressure-temperature single-crystal elastic properties of omphacite. *Journal of Geophysical Research: Solid Earth*, 126(5), e2021JB021683. <https://doi.org/10.1029/2021JB021683>
- Hunt, S. A., Whitaker, M. L., Bailey, E., Mariani, E., Stan, C. V., & Dobson, D. P. (2019). An experimental investigation of the relative strength of the silica polymorphs quartz, coesite, and stishovite. *Geochemistry, Geophysics, Geosystems*, 20(4), 1975–1989. <https://doi.org/10.1029/2018GC007842>
- Irfune, T. (1987). An experimental investigation of the pyroxene-garnet transformation in a pyrolite composition and its bearing on the constitution of the mantle. *Physics of the Earth and Planetary Interiors*, 45(4), 324–336. [https://doi.org/10.1016/0031-9201\(87\)90040-9](https://doi.org/10.1016/0031-9201(87)90040-9)
- Irfune, T., Sekine, T., Ringwood, A. E., & Hibberson, W. O. (1986). The eclogite-garnet transformation at high pressure and some geophysical implications. *Earth and Planetary Science Letters*, 77(2), 245–256. [https://doi.org/10.1016/0012-821X\(86\)90165-2](https://doi.org/10.1016/0012-821X(86)90165-2)
- Jacobsen, S. D., Liu, Z., Ballaran, T. B., Littlefield, E. F., Ehm, L., & Hemley, R. J. (2010). Effect of  $\text{H}_2\text{O}$  on upper mantle phase transitions in  $\text{MgSiO}_3$ : Is the depth of the seismic X-discontinuity an indicator of mantle water content? *Physics of the Earth and Planetary Interiors*, 183(1–2), 234–244. <https://doi.org/10.1016/j.pepi.2010.06.015>
- Jiang, F., Gwanmesia, G. D., Dyuzheva, T. I., & Duffy, T. S. (2009). Elasticity of stishovite and acoustic mode softening under high pressure by Brillouin scattering. *Physics of the Earth and Planetary Interiors*, 172(3–4), 235–240. <https://doi.org/10.1016/j.pepi.2008.09.017>
- Jiang, F., Speziale, S., & Duffy, T. S. (2004). Single-crystal elasticity of grossular- and almandine-rich garnets to 11 GPa by Brillouin scattering. *Journal of Geophysical Research*, 109(10), 1–10. <https://doi.org/10.1029/2004JB003081>

- Kaercher, P. M., Zepeda-Alarcon, E., Prakapenka, V. B., Kanitpanyacharoen, W., Smith, J. S., Sinogeikin, S. V., & Wenk, H.-R. (2015). Preferred orientation in experimentally deformed stishovite: Implications for deformation mechanisms. *Physics and Chemistry of Minerals*, 42(4), 275–285. <https://doi.org/10.1007/s00269-014-0718-5>
- Kemp, M., Jenkins, J., MacLennan, J., & Cottaar, S. (2019). X-discontinuity and transition zone structure beneath Hawaii suggests a heterogeneous plume. *Earth and Planetary Science Letters*, 527, 115781. <https://doi.org/10.1016/j.epsl.2019.115781>
- Knapp, N., Woodland, A. B., & Klimm, K. (2015). Experimental constraints on coesite abundances in eclogite and implications for the X seismic discontinuity. *Journal of Geophysical Research: Solid Earth*, 120(7), 4917–4930. <https://doi.org/10.1002/2015JB011933>
- Langenhorst, F., & Deutsch, A. (2012). Shock metamorphism of minerals. *Elements*, 8(1), 31–36. <https://doi.org/10.2113/gselements.8.1.31>
- Langrand, C., Hilairet, N., Nisr, C., Roskosz, M., Ribárik, G., Vaughan, G. B. M., & Merkel, S. (2017). Reliability of multigrain indexing for orthorhombic polycrystals above 1 Mbar: Application to MgSiO<sub>3</sub> post-perovskite. *Journal of Applied Crystallography*, 50(1), 120–130. <https://doi.org/10.1107/S1600576716018057>
- Leven, J. H. (1985). The application of synthetic seismograms to the interpretation of the upper mantle P-wave velocity structure in northern Australia. *Physics of the Earth and Planetary Interiors*, 38(1), 9–27. [https://doi.org/10.1016/0031-9201\(85\)90119-0](https://doi.org/10.1016/0031-9201(85)90119-0)
- Li, A., Fischer, K. M., van der Lee, S., & Wyssession, M. E. (2002). Crust and upper mantle discontinuity structure beneath eastern North America. *Journal of Geophysical Research*, 107(B5), 2100. <https://doi.org/10.1029/2001JB000190>
- Li, B., Rigden, S. M., & Liebermann, R. C. (1996). Elasticity of stishovite at high pressure. *Physics of the Earth and Planetary Interiors*, 96(2–3), 113–127. [https://doi.org/10.1016/0031-9201\(96\)03144-5](https://doi.org/10.1016/0031-9201(96)03144-5)
- Liermann, H.-P., Konôpková, Z., Morgenroth, W., Glazyrin, K., Bednarčík, J., McBride, E. E., et al. (2015). The Extreme conditions beam-line P02.2 and the Extreme conditions science infrastructure at PETRA III. *Journal of Synchrotron Radiation*, 22(4), 908–924. <https://doi.org/10.1107/S1600577515005937>
- Long, M. D., & Becker, T. W. (2010). Mantle dynamics and seismic anisotropy. *Earth and Planetary Science Letters*, 297(3–4), 341–354. <https://doi.org/10.1016/j.epsl.2010.06.036>
- Lutterotti, L., Matthies, S., Wenk, H.-R., Schultz, A. S., & Richardson, J. W. (1997). Combined texture and structure analysis of deformed limestone from time-of-flight neutron diffraction spectra. *Journal of Applied Physics*, 81(2), 594–600. <https://doi.org/10.1063/1.364220>
- Lutterotti, L., Vasin, R., & Wenk, H.-R. (2014). Rietveld texture analysis from synchrotron diffraction images. I. Calibration and basic analysis. *Powder Diffraction*, 29(1), 76–84. <https://doi.org/10.1017/S0885715613001346>
- Mainprice, D. (2009). Seismic anisotropy of the deep Earth from a mineral and rock physics perspective. In D. Mainprice (Ed.), *Treatise on Geophysics. Mineral Physics* (Vol. 2, pp. 437–491). Elsevier B.V.
- Mainprice, D., Bachmann, F., Hielscher, R., & Schaebe, H. (2015). Descriptive tools for the analysis of texture projects with large datasets using MTEX: Strength, symmetry and components. *Geological Society Special Publication*, 409(1), 251–271. <https://doi.org/10.1144/SP409.8>
- Mainprice, D., Bachmann, F., Hielscher, R., Schaebe, H., & Lloyd, G. E. (2015). Calculating anisotropic piezoelectric properties from texture data using the MTEX open source package. *Geological Society Special Publication*, 409(1), 223–249. <https://doi.org/10.1144/SP409.2>
- Masotta, M., Peres, S., Folco, L., Mancini, L., Rochette, P., Glass, B. P., et al. (2020). 3D X-ray tomographic analysis reveals how coesite is preserved in Muong Nong-type tektites. *Scientific Reports*, 10(1), 1–13. <https://doi.org/10.1038/s41598-020-76727-6>
- Massonne, H.-J. (2001). First find of coesite in the ultrahigh-pressure metamorphic area of the central Erzgebirge, Germany. *European Journal of Mineralogy*, 13(3), 565–570. <https://doi.org/10.1127/0935-1221/2001/0013-0565>
- McNamara, A. K., Karato, S. I., & Van Keken, P. E. (2001). Localization of dislocation creep in the lower mantle: Implications for the origin of seismic anisotropy. *Earth and Planetary Science Letters*, 191(1–2), 85–99. [https://doi.org/10.1016/S0012-821X\(01\)00405-8](https://doi.org/10.1016/S0012-821X(01)00405-8)
- McNamara, A. K., van Keken, P. E., & Karato, S.-I. (2003). Development of finite strain in the convecting lower mantle and its implications for seismic anisotropy. *Journal of Geophysical Research*, 108(B5), 1–14. <https://doi.org/10.1029/2002jb001970>
- Meissner, R., & Kern, H. (2011). In H. K. Gupta (Ed.), *Encyclopedia of Solid Earth Geophysics*. Springer Netherlands. <https://doi.org/10.1007/978-90-481-8702-7>
- Miyagi, L., & Wenk, H.-R. (2016). Texture development and slip systems in bridgmanite and bridgmanite + ferropericlae aggregates. *Physics and Chemistry of Minerals*, 43(8), 597–613. <https://doi.org/10.1007/s00269-016-0820-y>
- Mookherjee, M., Speziale, S., Marquardt, H., Jahn, S., Wunder, B., Koch-Müller, M., & Liermann, H.-P. (2015). Equation of state and elasticity of the 3.65 Å phase: Implications for the X-discontinuity. *American Mineralogist*, 100(10), 2199–2208. <https://doi.org/10.2138/am-2015-5312>
- Nippres, S. E. J., Kusznir, N. J., & Kendall, J. M. (2004). Modeling of lower mantle seismic anisotropy beneath subduction zones. *Geophysical Research Letters*, 31(19), 1–5. <https://doi.org/10.1029/2004GL020701>
- Nisr, C., Ribárik, G., Ungár, T., Vaughan, G. B. M., & Merkel, S. (2014). Three-dimensional X-ray diffraction in the diamond anvil cell: Application to stishovite. *High Pressure Research*, 34(2), 158–166. <https://doi.org/10.1080/08957959.2014.885021>
- Oddershede, J., Schmidt, S., Poulsen, H. F., Sørensen, H. O., Wright, J. P., & Reimers, W. (2010). Determining grain resolved stresses in polycrystalline materials using three-dimensional X-ray diffraction. *Journal of Applied Crystallography*, 43(3), 539–549. <https://doi.org/10.1107/S0021889810012963>
- Ono, S. (2008). Experimental constraints on the temperature profile in the lower mantle. *Physics of the Earth and Planetary Interiors*, 170(3–4), 267–273. <https://doi.org/10.1016/j.pepi.2008.06.033>
- Ono, S., Kikegawa, T., Higo, Y., & Tange, Y. (2017). Precise determination of the phase boundary between coesite and stishovite in SiO<sub>2</sub>. *Physics of the Earth and Planetary Interiors*, 264, 1–6. <https://doi.org/10.1016/j.pepi.2017.01.003>
- Prescher, C., & Prakapenka, V. B. (2015). DIOPTAS: A program for reduction of two-dimensional X-ray diffraction data and data exploration. *High Pressure Research*, 35(3), 223–230. <https://doi.org/10.1080/08957959.2015.1059835>
- Pugh, S., Jenkins, J., Boyce, A., & Cottaar, S. (2021). Global receiver function observations of the X-discontinuity reveal recycled basalt beneath hotspots. *Earth and Planetary Science Letters*, 561, 116813. <https://doi.org/10.1016/j.epsl.2021.116813>
- Rein, T., Hannemann, K., Thomas, C., & Korn, M. (2020). Location and characteristics of the X-discontinuity beneath SW Morocco and the adjacent shelf area using P-wave receiver functions. *Geophysical Journal International*, 223(3), 1780–1793. <https://doi.org/10.1093/gji/ggaa379>
- Renner, J., Stöckhert, B., Zerbán, A., Röller, K., & Rummel, F. (2001). An experimental study into the rheology of synthetic polycrystalline coesite aggregates. *Journal of Geophysical Research*, 106(B9), 19411–19429. <https://doi.org/10.1029/2001jb000431>
- Revenaugh, J., & Jordan, T. H. (1991). Mantle layering from ScS reverberations 3. The upper mantle. *Journal of Geophysical Research*, 96(B12), 19781–19810. <https://doi.org/10.1029/91jb01487>
- Saki, M., Thomas, C., Cobden, L., Abreu, R., & Buchen, J. (2019). Causes for polarity reversals of PP precursor waves reflecting off the 410 km discontinuity beneath the Atlantic. *Physics of the Earth and Planetary Interiors*, 286, 111–126. <https://doi.org/10.1016/j.pepi.2018.11.007>
- Saki, M., Thomas, C., Merkel, S., & Wookey, J. (2018). Detecting seismic anisotropy above the 410 km discontinuity using reflection coefficients of underside reflections. *Physics of the Earth and Planetary Interiors*, 274, 170–183. <https://doi.org/10.1016/j.pepi.2017.12.001>

- Schmerr, N. C. (2015). Imaging mantle heterogeneity with upper mantle seismic discontinuities. In *The Earth's heterogeneous mantle* (pp. 79–104). Springer International Publishing. [https://doi.org/10.1007/978-3-319-15627-9\\_3](https://doi.org/10.1007/978-3-319-15627-9_3)
- Schmerr, N. C., Kelly, B. M., & Thorne, M. S. (2013). Broadband array observations of the 300 km seismic discontinuity. *Geophysical Research Letters*, 40(5), 841–846. <https://doi.org/10.1002/grl.50257>
- Schmidt, S. (2014). GrainSpotter: A fast and robust polycrystalline indexing algorithm. *Journal of Applied Crystallography*, 47(1), 276–284. <https://doi.org/10.1107/S1600576713030185>
- Shen, G., & Lazor, P. (1995). Measurement of melting temperatures of some minerals under lower mantle pressures. *Journal of Geophysical Research*, 100(B9), 17699–17713. <https://doi.org/10.1029/95jb01864>
- Sørensen, H. O., Schmidt, S., Wright, J. P., Vaughan, G. B. M., Teichert, S., Garman, E. F., et al. (2012). Multigrain crystallography. *Zeitschrift für Kristallographie - Crystalline Materials*, 227(1), 63–78. <https://doi.org/10.1524/zkri.2012.1438>
- Tateno, S., Komabayashi, T., Hirose, K., Hirao, N., & Ohishi, Y. (2019). Static compression of B2 KCl to 230 GPa and its P-V-T equation of state. *American Mineralogist*, 104(5), 718–723. <https://doi.org/10.2138/am-2019-6779>
- Texier, M., & Cordier, P. (2006). TEM characterization of dislocations and slip systems in stishovite deformed at 14 GPa, 1, 300°C in the multianvil apparatus. *Physics and Chemistry of Minerals*, 33(6), 394–402. <https://doi.org/10.1007/s00269-006-0088-8>
- Tolédano, P., & Dmitriev, V. (1996). *Reconstructive phase transitions: In crystals and quasicrystals*. World Scientific. Retrieved from [https://books.google.de/books?hl=de&lr=&id=aw\\_XaQv7pBAC&oi=fnd&pg=PA1&dq=reconstructive+phase+transformation&ots=hQtrDG-fVID&sig=fcPWYMDIVspVvkxBoVY1\\_OOt07E#v=onepage&q&f=false](https://books.google.de/books?hl=de&lr=&id=aw_XaQv7pBAC&oi=fnd&pg=PA1&dq=reconstructive+phase+transformation&ots=hQtrDG-fVID&sig=fcPWYMDIVspVvkxBoVY1_OOt07E#v=onepage&q&f=false)
- Vavříček, V. (2006). Spatially dependent seismic anisotropy in the Tonga subduction zone: A possible contributor to the complexity of deep earthquakes. *Physics of the Earth and Planetary Interiors*, 155(1–2), 63–72. <https://doi.org/10.1016/j.pepi.2005.10.005>
- Wajeman, N. (1988). Detection of underside P reflections at mantle discontinuities by stacking broadband data. *Geophysical Research Letters*, 15(7), 669–672. <https://doi.org/10.1029/GL015i007p00669>
- Wang, Q., Burlini, L., Mainprice, D., & Xu, Z. (2009). Geochemistry, petrofabrics and seismic properties of eclogites from the Chinese Continental Scientific Drilling boreholes in the Sulu UHP terrane, eastern China. *Tectonophysics*, 475(2), 251–266. <https://doi.org/10.1016/j.tecto.2008.09.027>
- Wang, X., Liou, J. G., & Mao, H. K. (1989). Coesite-bearing eclogite from the Dabie Mountains in central China. *Geology*, 17(12), 1085. [https://doi.org/10.1130/0091-7613\(1989\)017<1085:cbeftd>2.3.co;2](https://doi.org/10.1130/0091-7613(1989)017<1085:cbeftd>2.3.co;2)
- Watt, J. P., Davies, G. F., & O'Connell, R. J. (1976). The elastic properties of composite materials. *Reviews of Geophysics*, 14(4), 541. <https://doi.org/10.1029/RG014i004p00541>
- Williams, Q., & Revenaugh, J. (2005). Ancient subduction, mantle eclogite, and the 300 km seismic discontinuity. *Geology*, 33(1), 1–4. <https://doi.org/10.1130/G20968.1>
- Woodland, A. B. (1998). The orthorhombic to high-P monoclinic phase transition in Mg-Fe pyroxenes: Can it produce a seismic discontinuity? *Geophysical Research Letters*, 25(8), 1241–1244. <https://doi.org/10.1029/98GL00857>
- Wright, J. P. (2005). ImageD11. Retrieved from <https://github.com/FABLE-3DXRD/ImageD11>
- Wu, Y., Fei, Y., Jin, Z., & Liu, X. (2009). The fate of subducted upper continental crust: An experimental study. *Earth and Planetary Science Letters*, 282(1–4), 275–284. <https://doi.org/10.1016/j.epsl.2009.03.028>
- Xu, F., Vidale, J. E., Earle, P. S., & Benz, H. M. (1998). Mantle discontinuities under southern Africa from precursors to  $P'P'$ . *Geophysical Research Letters*, 25(4), 571–574. <https://doi.org/10.1029/98GL010122>
- Xu, F., Yamazaki, D., Tsujino, N., & Guan, L. (2020). Lattice preferred orientation of stishovite deformed at high pressure and high temperature. *Physics of the Earth and Planetary Interiors*, 306, 106546. <https://doi.org/10.1016/j.pepi.2020.106546>
- Yang, R., & Wu, Z. (2014). Elastic properties of stishovite and the  $\text{CaCl}_2$ -type silica at the mantle temperature and pressure: An ab initio investigation. *Earth and Planetary Science Letters*, 404, 14–21. <https://doi.org/10.1016/j.epsl.2014.07.020>
- Zhang, J. F., Shi, F., Xu, H. J., Wang, L., Feng, S. Y., Liu, W. L., et al. (2013). Petrofabric and strength of  $\text{SiO}_2$  near the quartz-coesite phase boundary. *Journal of Metamorphic Geology*, 31(1), 83–92. <https://doi.org/10.1111/jmg.12006>
- Zhang, Z., & Lay, T. (1993). Investigation of upper mantle discontinuities near northwestern Pacific subduction zones using precursors to  $sSH$ . *Journal of Geophysical Research*, 98(B3), 4389–4405. <https://doi.org/10.1029/92jb02050>
- Zoeppritz, K. (1919). On the reflection and penetration of seismic waves through unstable layers. *Göttinger Nachrichten*, 1, 66–84.

## References From the Supporting Information

- Akaogi, M., Oohata, M., Kojitani, H., & Kawaji, H. (2011). Thermodynamic properties of stishovite by low-temperature heat capacity measurements and the coesite-stishovite transition boundary. *American Mineralogist*, 96(8–9), 1325–1330. <https://doi.org/10.2138/am.2011.3748>
- Fischer, R. A., Campbell, A. J., Chidester, B. A., Reaman, D. M., Thompson, E. C., Pigott, J. S., et al. (2018). Equations of state and phase boundary for stishovite and  $\text{CaCl}_2$ -type  $\text{SiO}_2$ . *American Mineralogist*, 103(5), 792–802. <https://doi.org/10.2138/am-2018-6267>
- Gonzalez-Platas, J., Alvaro, M., Nestola, F., & Angel, R. J. (2016). EosFit7-GUI: A new graphical user interface for equation of state calculations, analyses and teaching. *Journal of Applied Crystallography*, 49(4), 1377–1382. <https://doi.org/10.1107/S1600576716008050>
- Hao, M., Zhang, J. S., Pierotti, C. E., Ren, Z., & Zhang, D. (2019). High-pressure single-crystal elasticity and thermal equation of state of omphacite and their implications for the seismic properties of eclogite in the Earth's interior. *Journal of Geophysical Research: Solid Earth*, 124(3), 2368–2377. <https://doi.org/10.1029/2018JB016964>
- Irifune, T., Higo, Y., Inoue, T., Kono, Y., Ohfuji, H., & Funakoshi, K. (2008). Sound velocities of majorite garnet and the composition of the mantle transition region. *Nature*, 451(7180), 814–817. <https://doi.org/10.1038/nature06551>
- Kono, Y., Higo, Y., Ohfuji, H., Inoue, T., & Irifune, T. (2007). Elastic wave velocities of garnetite with a MORB composition up to 14 GPa. *Geophysical Research Letters*, 34(14), 1–5. <https://doi.org/10.1029/2007GL030312>
- Kung, J., Li, B., Uchida, T., & Wang, Y. (2005). In-situ elasticity measurement for the unquenchable high-pressure clinopyroxene phase: Implication for the upper mantle. *Geophysical Research Letters*, 32(1), 2–5. <https://doi.org/10.1029/2004GL021661>
- Nishihara, Y., Aoki, I., Takahashi, E., Matsukage, K. N., & Funakoshi, K. (2005). Thermal equation of state of majorite with MORB composition. *Physics of the Earth and Planetary Interiors*, 148(1), 73–84. <https://doi.org/10.1016/j.pepi.2004.08.003>
- Sanchez-Valle, C., Sinogeikin, S. V., Smyth, J. R., & Bass, J. D. (2008). Sound velocities and elasticity of DHMS phase A to high pressure and implications for seismic velocities and anisotropy in subducted slabs. *Physics of the Earth and Planetary Interiors*, 170(3–4), 229–239. <https://doi.org/10.1016/j.pepi.2008.07.015>
- Zha, C. S., Duffy, T. S., Downs, R. T., Mao, H. K., & Hemley, R. J. (1998). Brillouin scattering and X-ray diffraction of San Carlos olivine: Direct pressure determination to 32 GPa. *Earth and Planetary Science Letters*, 159(1–2), 25–33. [https://doi.org/10.1016/S0012-821X\(98\)00063-6](https://doi.org/10.1016/S0012-821X(98)00063-6)